ACS APPLIED MATERIALS & INTERFACES

www.acsami.org

Research Article

A Multimodal Nanoplatform Integrating Photodynamic Therapy and Wnt/β-Catenin Inhibition Reprograms the Tumor Microenvironment to Potentiate Immune Checkpoint Therapy in Triple-Negative Breast Cancer

Lingjun Zeng,[§] Kaiqin You,[§] Mingjian Lu, Xiaomu Hu, Changqing Zheng, Lingyan Yao, Bingkun Kang, Shuang Lin, Xiaoliang Deng, Jia Yan,* and Xin Zhou*

Cite This: https://doi.org/10.1021/acsami.5c04799

Read Online

ACCESS | Metrics & More | Article Recommendations | Supporting Information

ABSTRACT: The immunosuppressive tumor microenvironment (TME) poses a critical barrier to the efficacy of immune checkpoint inhibitors in triple-negative breast cancer (TNBC). Here, we report a self-assembled polymeric nanoplatform coloading the photosensitizer verteporfin and the Wnt/β-catenin inhibitor XAV-939. This dual-functional system enhanced cellular uptake and potentiated photodynamic therapy (PDT)-induced immunogenic cell death, while simultaneously downregulating β-catenin signaling to reverse immunosuppression. In vivo, the nanoplatform substantially improved therapeutic outcomes, converting "cold" tumors into immune-responsive phenotypes characterized by augmented dendritic cell maturation, increased cytotoxic T cell infiltration, reduced regulatory T cell abundance, and enhanced proinflammatory cytokine release. Combined with PD-L1 blockade, this strategy synergistically activated systemic antitumor immunity, resulting in primary tumor regression, metastasis reduction, and systemic abscopal effects against distal tumors. These results highlight the promise of targeted TME reprogramming as a strategy to overcome TNBC's recalcitrance to immunotherapy.

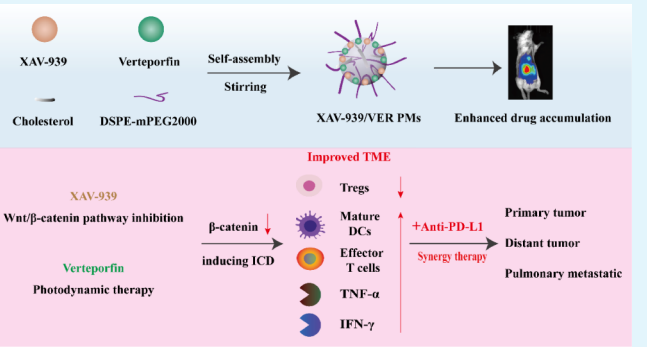

KEYWORDS: *triple-negative breast cancer, tumor microenvironment, immune checkpoint inhibitors, photodynamic therapy, Wnt/β-catenin signaling pathway*

1. INTRODUCTION

According to the Global Cancer Statistics 2022, breast cancer continues to have the highest incidence and mortality rates among female malignancies, among which triple-negative breast cancer (TNBC) constitutes 15−20% of diagnoses yet accounts for 35% of breast cancer-related deaths.[1] TNBC represents the most aggressive subtype of breast cancer, distinguished by its limited therapeutic options, poor prognosis, and elevated mortality rates.[2,3] Conventional treatments for TNBC include surgery, radiotherapy, and chemotherapy.[4,5] However, these modalities present varying degrees of safety and efficacy limitations, resulting in suboptimal clinical outcomes.[6] In recent years, immunotherapy, which harnesses the body's immune system to identify and eradicate tumor cells, has emerged as one of the most promising cancer treatment strategies.[7] Immune checkpoint inhibitors (ICIs) have demonstrated some clinical efficacy in the management of TNBC.[8] Nonetheless, the response rate of TNBC to ICIs remains limited.[9,10] The therapeutic recalcitrance stems not only from molecular heterogeneity but also from the immunosuppressive tumor microenvironment (TME) characteristic of TNBC. This environment is marked by low tumor immunogenicity, a paucity of mature antigen-presenting cells (APCs), reduced lymphocyte infiltration, elevated levels of immunosuppressive cell infiltration, and dysregulated chemokine and cytokine expression within the tumor tissue, rendering TNBC a prototypical "cold" tumor.[11] Consequently, transforming the "cold" phenotype of TNBC is crucial for enhancing its responsiveness to ICIs.

Photodynamic therapy (PDT)-induced immunogenic cell death (ICD) presents a promising strategy to convert "cold" tumors into "hot" ones.[12] During PDT, photosensitizers localized within the tissue generate cytotoxic reactive oxygen species (ROS) upon exposure to light. The potent oxidative

Received: March 9, 2025
Revised: May 25, 2025
Accepted: May 26, 2025

Scheme 1. Schematic Illustration of the Preparation of XAV-939/VER PMs, and their Application in Improving the Efficacy of ICIs in TNBC through PDT Combined with the Downregulation of the Wnt/β-Catenin Signaling Pathway

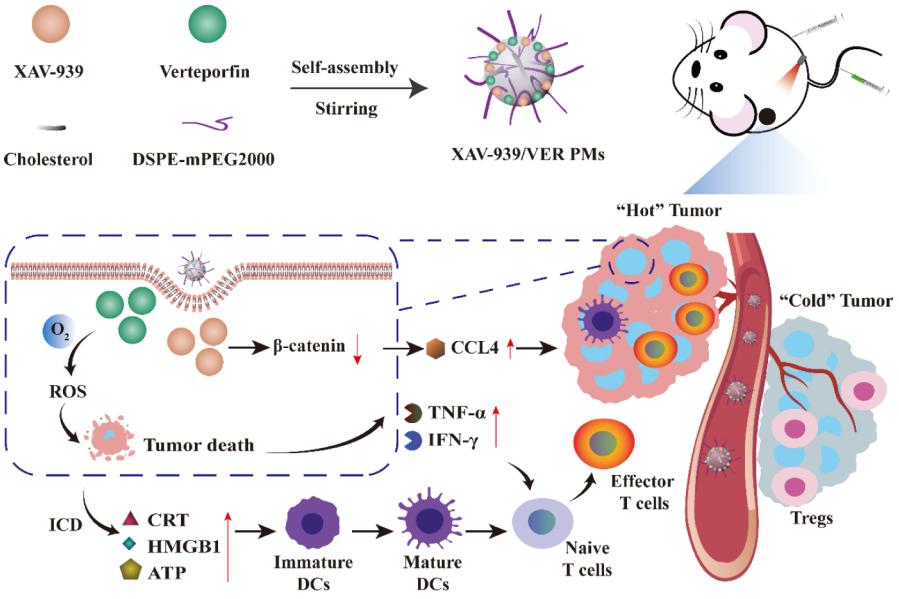

effects of ROS induce tumor cell death, facilitate the release of tumor-associated antigens, and enhance tumor immunogenicity. This process also triggers the release of damage-associated molecular patterns (DAMPs) from the dying tumor cells, which serve to activate, differentiate, and mature APCs.[13] Furthermore, PDT can stimulate the release of chemokines, thereby promoting the infiltration of lymphocytes and APCs into the tumor.[14] PDT has been identified as an immunostimulatory approach that may enhance the tumor response rate to ICIs. Empirical evidence suggests that the combination of PDT with PD-L1 inhibitors can extend survival in tumor-bearing mice.[15] Verteporfin (VER), a second-generation photosensitizer, is approved by the FDA for the PDT treatment of age-related macular degeneration. VER exhibits an absorption peak at approximately 690 nm within the near-infrared light spectrum, which offers superior tissue penetration and reduced tissue damage compared to ultraviolet and visible light.[16]

Complementing PDT's immunological priming, Wnt/β-catenin pathway inhibition emerges as a strategic countermeasure against TME immunosuppression. Researches indicate that the Wnt/β-catenin signaling pathway is intricately involved in the initiation, progression, and immune evasion of malignant tumors.[17,18] β-catenin, the central protein of this pathway, is typically expressed at low levels in normal cells but can accumulate aberrantly in tumor cells.[19,20] Furthermore, β-catenin is associated with reduced lymphocyte infiltration in numerous "cold" tumors. One of the primary mechanisms by which β-catenin inhibits lymphocyte infiltration into tumor tissue is through the reduction of tumor cell secretion of the chemokine CCL4.[21] CCL4, a chemotactic factor, is a crucial component in the immune-tumor interaction network. It facilitates the infiltration of APCs into the tumor. APCs are essential for initiating an effective antitumor immune response. Shanthi's research identified aberrations in the Wnt/β-catenin signaling pathway in breast cancer, characterized by elevated β-catenin expression.[22] The downregulation of β-catenin expression via small interfering RNA has been shown to inhibit breast cancer growth in murine models and demonstrates synergistic antitumor effects when combined with ICIs. XAV-939, a potent inhibitor of the Wnt/β-catenin signaling pathway, selectively impedes Wnt/β-catenin-mediated transcription by targeting tankyrase1/2.[23] This compound inhibits the poly-ADP-ribosylation of Axin1, thereby reducing its proteasomal degradation.[24] Axin1 is a critical component of the β-catenin degradation complex, facilitating the proteasomal degradation of β-catenin.

The intricate mechanisms underlying the formation of "cold" tumors often render a singular therapeutic approach inadequate for modifying their immunologically inert characteristics.[25] Here, this study reports a novel approach integrating PDT-induced ICD with Wnt/β-catenin pathway inhibition to convert TNBC into an immunoresponsive "hot" tumor phenotype, thereby enhancing ICIs efficacy. The hydrophobicity and poor tumor-targeting of XAV-939 and VER limit their clinical translation. Polymeric micelles (PMs) present a promising strategy to address these limitations. PMs are formed through the self-assembly of amphiphilic block copolymers, wherein the hydrophobic segments create an inner core that can encapsulate hydrophobic drugs, while the hydrophilic segments form an outer shell that interfaces with aqueous environments.[26,27] PMs can preferentially accumulate in tumor tissues via the enhanced permeability and retention (EPR) effect. Furthermore, the incorporation of polyethylene glycol (PEG) as a hydrophilic block can reduce recognition by the reticuloendothelial system, thereby prolonging blood circulation time and increasing drug accumulation in tumor tissues. The remarkable stability, biocompatibility, biodegradability, and low toxicity of PMs have established it as a promising platform for the delivery of anticancer drugs. Our research group has previously explored the formulation and preparation of XAV-939 and VER coloaded PMs (XAV-939/VER PMs).[28] The optimized XAV-939/VER PMs demonstrated a small particle size, high encapsulation efficiency, and robust stability.

This study hypothesizes that XAV-939/VER PMs will achieve dual therapeutic effects. VER-mediated PDT generates ROS to induce ICD, releasing tumor antigens and DAMPs to

https://doi.org/10.1021/acsami.5c04799
ACS Appl. Mater. Interfaces XXXX, XXX, XXX−XXX

activate dendritic cells (DCs). Activated DCs then play a vital role in presenting tumor antigens to T cells, thereby priming the immune system for an antitumor response. XAV-939 disrupts β-catenin signaling, upregulating chemokine CCL4 to recruit cytotoxic T cells while reducing Treg infiltration. The combination aims to synergistically reprogram the TME, thereby sensitizing TNBC to PD-L1 blockade (Scheme 1).

2. EXPERIMENTAL SECTION

2.1. Materials. VER was purchased from the United States Pharmacopeial Convention (USA). XAV-939 was obtained from MedChemExpress (USA). DSPE-mPEG2000 and cholesterol were obtained from AVT Pharmaceutical Co. (China). Roswell Park Memorial Institute (RMPI) 1640, phosphate-buffered saline (PBS), 3-(4,5-dimethylthiazol-2-yl)-2,5-diphenyltetrazolium bromide (MTT), and CalceinAM/PI staining kit were obtained from Jiangsu Keygen Biotech Corp. (China). Fetal bovine serum (FBS) and trypsin-EDTA were obtained from Thermo Fisher Scientific Co. (USA). The reactive oxygen species detection kit and ATP assay Kit were obtained from Beijing Soleberg Technology Co. (China). Annexin V-APC/PI Apoptosis Detection Kit was obtained from Wuhan Eliot Biotechnology Co. (China). Calcein/PI cell viability/cytotoxicity assay kit and BCA protein concentration assay kit were obtained from Shanghai Biyuntian Biotechnology Co. (China). Anti-CRT-Alexa Fluor 488 and anti-HMGB1-FITC were obtained from Beijing Bioss Biotechnology Co. (China). Anti-β-catenin and anti-β-actin were obtained from Abclonal Biotechnology Co. (China). Mouse CCL4/MIP-1 beta ELISA KIT was obtained from Absin (China). Anti-PD-L1 was donated by Kangfang Pharmaceutical Co. (China). Anti-CD3-PE, anti-CD4-APC, anti-CD8-FITC, anti-CD11c-PE-Cy7, anti-CD45-APC-Cy7, anti-CD80-PE, anti-CD86-APC, anti-MHC-II- FITC, 7-AAD-Percp, and mouse BD FC block were provided by BD Biosciences (USA). Mouse TNF-alpha ELISA kit and mouse IFN-gamma ELISA kit were obtained from Hangzhou Lianke Biotechnology Co. (China).

2.2. Preparation of xav-939/VER PMs. The preparation of XAV-939/VER PMs was conducted following the previously established protocol, with all procedures carried out under dark conditions.[28] Initially, XAV-939 (400 μg), VER (100 μg), DSPE-mPEG2000 (1666.7 μg), and cholesterol (833.3 μg) were dissolved in 200 μL of DMF to constitute the organic phase. This organic phase was gradually introduced into 4 mL of purified water under magnetic stirring at 1000 rpm at ambient temperature. After 60 min of stirring, the resultant solution was transferred into an ultrafiltration centrifuge tube (MWCO 10 000) and subjected to five washes with normal saline.

2.3. Characterization of XAV-939/VER PMs. The morphological feature of XAV-939/VER PMs was characterized using transmission electron microscopy (TEM, JEM2100F, JEOL, Japan) after negative staining with 1% phosphotungstic acid. The particle size, polydispersity index (PDI), and zeta potential of the nanoparticles were analyzed by dynamic light scattering (DLS, Zetasizer Lab, Malvern, UK) at 25 °C. The encapsulation efficiency (EE, expressed as a percentage) of XAV-939 and VER was determined using high-performance liquid chromatography (HPLC, Agilent 1200, USA). EE was calculated as the ratio of the mass of the drug encapsulated in XAV-939/VER PMs to the initial mass of the added drug. For XAV-939/VER PMs, systematic spectrophotometric analysis was conducted. This involved ultraviolet−visible (UV−vis) absorption spectroscopy within the wavelength range of 200−800 nm and fluorescence emission spectroscopy with an excitation wavelength of 427 nm. To investigate the formation mechanism of the nanoparticles, the effects of adding different concentrations (10, 20, 40, 80 mmol/L) of urea (a hydrogen bond disruptor), Tween-20 (a hydrophobic interaction disruptor), and sodium dodecyl sulfate (SDS, also a hydrophobic interaction disruptor) on the dissociation of nanoparticles were examined. The UV−vis absorption spectra of free VER and XAV-939/VER PMs were recorded after 15 min irradiation with a 660 nm laser at an intensity of 0.3 W/cm^2 to evaluate the stability of XAV-939/VER PMs under laser illumination. Furthermore, the stability of XAV-939/VER PMs in PBS supplemented with 10% fetal bovine serum (FBS) was assessed by monitoring the particle size and PDI over a period of 5 days using DLS. The in vitro drug release profiles were evaluated by the dialysis membrane method (MWCO 14000 Da). The experiments were performed in phosphate-buffered saline (PBS, pH 5.5, 6.5, 7.4) containing 0.2% (w/v) Tween-20 under sink conditions at 37 °C, with continuous agitation at 100 rpm.

2.4. Cell Culture. The 4T1 mouse cell line was obtained from the Cell Resource Center of the Shanghai Institute of Biological Sciences, Chinese Academy of Sciences (Shanghai, China). The 4T1 cells were cultured in RPMI 1640 medium, supplemented with 10% fetal bovine serum, 80 U/mL penicillin, and 80 μg/mL streptomycin, in a humidified atmosphere at 37 °C with 5% CO_2.

2.5. Cellular Uptake and Cellular Uptake Mechanism Analysis. In vitro cellular uptake was evaluated using fluorescence microscopy (IX73, Olympus, Japan) and flow cytometry (FC500, BD, USA). The 4T1 cells were seeded in a 6-well plate at a density of 3 × 10^5 cells per well. Following overnight incubation, the culture medium was replaced with fresh medium containing either free VER or XAV-939/VER PMs, maintaining an equivalent VER concentration of 0.36 μg/mL. Cells were subsequently incubated for 30, 60, or 120 min and examined using fluorescence microscopy. Similarly, 4T1 cells were treated with free VER or XAV-939/VER PMs as previously described. Post incubation for 30, 60, or 120 min, the cells were trypsinized, resuspended in 300 μL of PBS, and analyzed via flow cytometry. To evaluate the influence of drug concentration on cellular uptake, 4T1 cells were exposed to varying concentrations of free VER or XAV-939/VER PMs, specifically 0.18, 0.36, and 0.72 μg/mL of VER. After a 120 min incubation period, cellular uptake was assessed as previously outlined. The mechanism of uptake for XAV-939/VER PMs was further explored using different endocytosis inhibitors. Cells were pretreated with colchicine (8 μg/mL), genistein (50 μg/mL), chlorpromazine (5 μg/mL), or 2-deoxy-D-glucose (8 mg/mL) for 60 min, followed by the addition of XAV-939/VER PMs (VER concentration of 0.72 μg/mL) and an additional 120 min incubation. Cells that were not treated with the inhibitor were used as a control group.

2.6. Dark Cytotoxicity and Phototoxicity Evaluations. The cytotoxic effects of XAV-939/VER PMs in the absence of laser irradiation were assessed using the MTT assay. For this purpose, 4T1 cells were seeded in a 96-well plate at a density of 5 × 10^3 cells per well. Following an overnight incubation period, the culture medium was replaced with fresh medium containing varying concentrations of either free XAV-939, free VER, or XAV-939/VER PMs. After 24 h of incubation, cell

https://doi.org/10.1021/acsami.5c04799
ACS Appl. Mater. Interfaces XXXX, XXX, XXX−XXX

viability was measured via the MTT assay. In a parallel experiment, 4T1 cells were treated with the same agents as described above. After 2 h of incubation in the dark, cells in the free VER and XAV-939/VER PMs groups were subjected to irradiation with a 660 nm laser for 10 min at a power density of 0.3 W/cm^2. After an additional 22-h incubation, cell viability was evaluated using the MTT assay to determine the phototoxic effects of the treatments.

2.7. In Vitro Cell Apoptosis Detection Assay. Cell apoptosis was analyzed through flow cytometry utilizing the Annexin V-APC/7-AAD apoptosis detection kit. For this analysis, 4T1 cells were seeded in a 6-well plate at a density of 3×10^5 cells per well. After overnight incubation, the medium was replaced with fresh medium containing either free XAV-939, free VER, or XAV-939/VER PMs. The concentrations of XAV-939 and VER in all media containing these compounds were maintained at 2.88 μg/mL and 0.72 μg/mL, respectively. Following a 2-h incubation period in the dark, cells in the free VER and XAV-939/VER PMs treatment groups were subjected to laser irradiation as previously described. Subsequently, after an additional 22-h incubation, cells were harvested, stained, and analyzed via flow cytometry.

2.8. Live/Dead Staining Assay. The viability of the cells was assessed using a fluorescence microscope in conjunction with the Calcein-AM/PI staining kit. For this experiment, 4T1 cells were seeded in a 6-well plate at a density of 3×10^5 cells per well. The cells were then grouped and treated according to the protocol outlined in the In Vitro Cell Apoptosis Detection Assay section. Following laser irradiation and an additional 4-h incubation, cells were stained, and live (green) and dead (red) cells were visualized using a fluorescence microscope.

2.9. In Vitro ROS Measurement. Intracellular ROS levels were quantified by flow cytometry employing DCFH-DA as the fluorescent probe. 4T1 cells were seeded into a 6-well plate at a density of 3×10^5 cells per well, grouped, and treated as described in the In Vitro Cell Apoptosis Detection Assay section. Postlaser irradiation, the culture medium was immediately removed, and the cells were washed three times with PBS. The fluorescence probe DCFH-DA was introduced to the cells and incubated at 37 °C for 30 min. Subsequently, the cells were harvested and analyzed via flow cytometry.

2.10. In Vitro Immunogenic Cell Death Assay. 4T1 cells were seeded into a 6-well plate at a density of 3×10^5 cells per well. The cells were categorized and treated as outlined in the In Vitro Cell Apoptosis Detection Assay section. For the detection of CRT and HMGB1, following laser irradiation and an additional 4-h incubation, the cells were washed three times with PBS and fixed with 4% paraformaldehyde. Subsequently, the cells were stained with Alexa Fluor 488-conjugated CRT or HMGB1/FITC antibodies and examined using a fluorescence microscope. For ATP detection, after laser irradiation and a further 4-h incubation, the cells were collected and lysed. Intracellular ATP levels were quantified using an ATP assay kit.

2.11. β-Catenin and CCL4 Detection. 4T1 cells were seeded into a 6-well plate at a density of 3×10^5 cells per well. The cells were categorized and treated as specified in the In Vitro Cell Apoptosis Detection Assay section. Following laser irradiation and an additional 22-h incubation, the cell culture supernatants were collected, and CCL4 levels in the supernatants were measured using a CCL4 ELISA kit. Cells were lysed utilizing a cell lysis buffer supplemented with a variety of protease inhibitors. Subsequently, the β-catenin levels were quantified through Western blot analysis.

2.12. Establishment of 4T1 Subcutaneous Tumor Models. A subcutaneous 4T1 tumor model was developed to investigate the impact of PDT and the downregulation of the Wnt/β-catenin signaling pathway on the efficacy of ICIs in TNBC. All animal experiments were performed in compliance with the guidelines of the Animal Care and Use Committee of the 900th Hospital of PLA Joint Logistic Support Force. Female BALB/c mice were employed to establish the subcutaneous 4T1 tumor model for in vivo imaging and assessment of antitumor activity. Specifically, 4T1 cells (1×10^6) suspended in 100 μL of PBS were injected subcutaneously into the right flank of the mice. Tumor volume was calculated using the formula: $V = (W^2 \times L)/2$, where V represents the tumor volume, W denotes the tumor width, and L indicates the tumor length. The relative tumor volume was defined as V/V0, where V0 is the initial volume.

2.13. In Vivo Tumor Imaging and Biodistribution. Upon the tumor reaching a size of 50−100 mm^3, free VER and XAV-939/VER PMs were administered via tail vein injection. The equivalent doses of VER and XAV-939 in the different formulations were 2.5 mg/kg and 10 mg/kg, respectively. Mice were subjected to imaging at intervals of 0.5, 1, 2, 3, 4, 6, 8, 12, and 24 h following injection, utilizing a small animal in vivo imaging system (AniView100, Biolight Biotechnology Co., Ltd., Guangzhou, China). Subsequently, the primary organs, including the heart, liver, spleen, lung, and kidney, as well as tumors, were excised for ex vivo imaging after the mice were euthanized.

2.14. Evaluation of Primary Antitumor Effects. Upon reaching a tumor size of 50−100 mm^3, 4T1 tumor-bearing mice were randomly allocated into seven distinct groups: saline, XAV-939, anti-PD-L1, XAV-939 plus anti-PD-L1, VER plus laser, VER plus anti-PD-L1 plus laser, and XAV-939/VER PMs plus anti-PD-L1 plus laser. The equivalent dosages of XAV-939, VER, and anti-PD-L1 administered across the groups were 10 mg/kg, 2.5 mg/kg, and 10 mg/kg, respectively. Administration of XAV-939 and anti-PD-L1 was performed via intraperitoneal injection, while the remaining groups received treatments through tail vein injection. Treatments were conducted on days 1, 4, 7, and 10. For groups receiving laser treatment, exposure to light (200 mW/cm^2 for 5 min) occurred 2 h postdrug administration. Mouse body weight and tumor volume were monitored every other day.

2.15. In Vivo Immune Response and Cytokines Evaluation. On day 12, blood samples were collected via ocular puncture for serum preparation. Levels of TNF-α and IFN-γ were quantified using an ELISA assay kit. After sacrificing the mice, inguinal lymph nodes and spleens were harvested. Flow cytometry analysis was employed to ascertain the percentage of mature dendritic cells (DCs) in the lymph nodes and CD8+ T cells in the spleen. Tumor tissues were excised, weighed, and photographed for further analysis. Immunohistochemical analysis was conducted to assess the expression levels of CD8+ and Foxp3+ markers within tumor tissues.

2.16. Evaluation of Distal Antitumor Effects. In this study, mice were concurrently inoculated with two distinct 4T1 tumors on both the left and right flanks to create a model of distant tumor growth. Upon reaching a tumor volume of 50−100 mm^3, the mice received treatments with saline, XAV-939, anti-PD-L1, XAV-939 plus anti-PD-L1, VER plus laser, VER plus anti-PD-L1 plus laser, or XAV-939/VER PMs plus anti-PD-L1 plus laser, as outlined in the "Evaluation of Primary

https://doi.org/10.1021/acsami.5c04799
ACS Appl. Mater. Interfaces XXXX, XXX, XXX−XXX

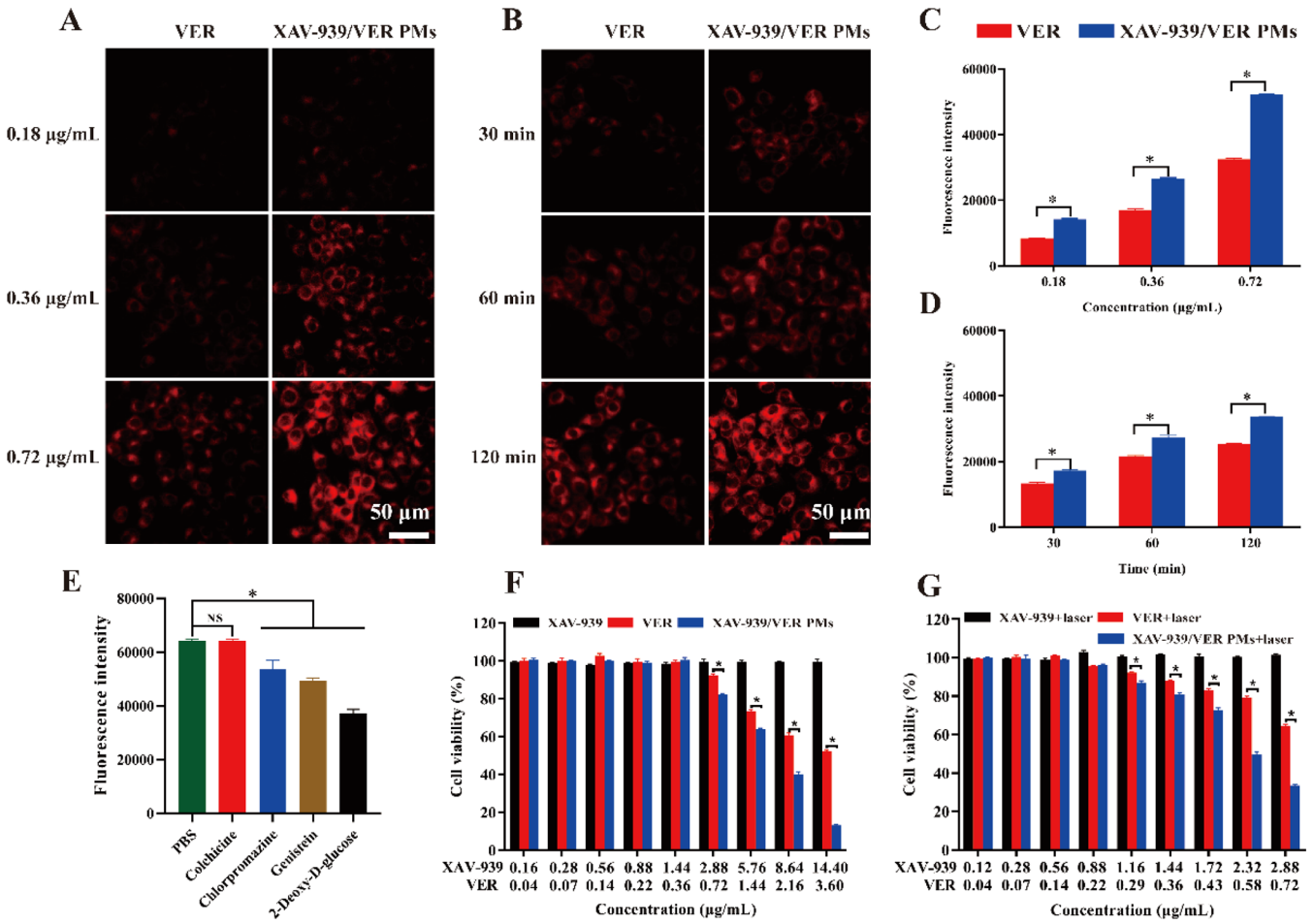

Figure 1. Cellular uptake of free VER and XAV-939/VER PMs by 4T1 cells at different concentrations of VER (0.18, 0.36, 0.72 μg/mL) by (A) fluorescence microscopy and (C) flow cytometry, scale bar: 50 μm. Cellular uptake of free VER and XAV-939/VER PMs by 4T1 cells at 30, 60, and 120 min by (B) fluorescence microscopy and (D) flow cytometry. (E) Cellular uptake of XAV-939/VER PMs by 4T1 cells in the presence of different endocytic inhibitors by flow cytometry. (F-G) Cell viability of 4T1 cells treated with different concentrations of XAV-939, VER, and XAV-939/VER PMs with or without laser irradiation (660 nm, 0.3 W/cm^2, 10 min).

Anti-Tumor Effects" section. On day 12, post-treatment, the mice were euthanized, and tumor tissues were excised, weighed, and photographed for further analysis. Immunohistochemistry was employed to investigate CD8+ and Foxp3+ expression in the distant tumors.

2.17. Evaluation of Antipulmonary Metastatic Effects. Once the tumors achieved a size of 50−100 mm^3, the mice were randomly allocated into seven experimental groups, with the grouping and treatment protocols detailed in the "Evaluation of Primary Anti-Tumor Effects" section. One day prior to the initial treatment, approximately 5×10^5 4T1 cells were administered via tail vein injection to establish a lung metastasis model. On day 25, the mice were sacrificed, and lung tissues were harvested for analysis. The number of tumor metastases in lung tissue was documented, and HE staining was conducted on the lung sample.

2.18. Statistical Analysis. All experiments were performed a minimum of three times. Data are presented as mean ± standard deviation (SD). Statistical analyses were conducted using SPSS version 13.0 (SPSS Inc., USA), employing one-way analysis of variance (ANOVA) for data comparison. Statistical significance was determined as follows: not significant (NS) for $p > 0.05$, and significant (*) for $p < 0.05$.

3. RESULTS AND DISCUSSION

3.1. Characterization of XAV-939/VER PMs. As shown in Figure S1A, the nanoparticles exhibit a regular spherical structure with no obvious aggregation, indicating good monodispersity. DLS analysis (Figure S1B) revealed that the nanoparticles had a hydrodynamic diameter of 85.36 ± 1.62 nm with a PDI of 0.13 ± 0.05. A PDI value below 0.2 confirms the monodisperse nature of the system, consistent with the homogeneous size distribution observed by TEM. The nanoparticles exhibited a zeta potential of −42.83 ± 2.73 mV (Figure S1C). According to DLVO theory, the high zeta potential value effectively inhibits particle aggregation by enhancing interparticle electrostatic repulsion, which significantly contributes to the colloidal stability of the nanosystem. The results of the encapsulation efficiency assay showed that the EE of XAV-939 and VER were (98.37 ± 1.26)% and (96.25 ± 1.83)%, respectively.

This study systematically characterized the nanoformulation using UV−vis absorption and fluorescence emission spectroscopy. As shown in Figure S1D, the XAV-939/VER PMs exhibited distinct absorption peaks at 288 and 427 nm, corresponding to XAV-939 and VER, respectively. Notably, XAV-939/VER PMs in aqueous medium demonstrated reduced absorbance at characteristic peaks compared to free

https://doi.org/10.1021/acsami.5c04799
ACS Appl. Mater. Interfaces XXXX, XXX, XXX−XXX

drugs dissolved in methanol. Similar observations were made in fluorescence emission spectra analysis (Figure S1E), where the XAV-939/VER PMs demonstrated significantly lower fluorescence intensity compared to free VER. These phenomena may be attributed to the physical shielding effect of the carrier material. Collectively, these spectroscopic evidence validate the successful encapsulation of drug molecules within the PMs system.

As shown in Figure S1F, treatment with Tween-20 and SDS significantly reduced the particle size of the nanoparticles, indicating characteristic micellar disintegration. In contrast, urea treatment induced no notable changes in particle size, suggesting that hydrogen bonding interactions played a limited role in nanoparticle assembly. These chemical dissociation experiments revealed that the formation of XAV-939/VER PMs follows a hydrophobic interaction-dominated energy-driven mechanism.

As depicted in Figure S1G, free VER exhibited pronounced photolabile properties under laser irradiation, showing a time-dependent decline in UV−vis absorption intensity, which was quantitatively attributed to photodegradation processes. In contrast, XAV-939/VER PMs demonstrated exceptional photostability under identical irradiation conditions (Figure S1H), with negligible fluctuation in absorption intensity. These results indicate that encapsulating VER within nanoparticles substantially enhances its photostability. The nanoparticle matrix likely serves as a physical barrier, shielding VER from direct exposure to laser photons and thereby minimizing photodegradation occurrence.

To evaluate the physiological stability of XAV-939/VER PMs, the colloidal behavior of nanoparticles was monitored in PBS containing 10% FBS over 5 days using DLS (Figure S1I,J). Results demonstrated that the nanoparticles maintained excellent stability, with hydrodynamic diameter increasing only marginally from 85.36 ± 1.62 nm to 98.45 ± 2.13 nm during the observation period. The PDI remained stable within a narrow range of 0.13−0.17, and no visible flocculation or precipitation was observed. This superior stability originates from synergistic effects: (1) Strong electrostatic repulsion generated by the high surface electronegativity; (2) Effective suppression of nonspecific serum protein adsorption through steric hindrance conferred by the polyethylene glycol (PEG) corona.

The drug release profile of XAV-939/VER PMs was systematically investigated in PBS buffer systems simulating physiological pH environments (5.5, 6.5, 7.4) over a 48-h period (Figure S1K,L). Results demonstrated that XAV-939/VER PMs exhibited significant dual-dependent release characteristics governed by time and pH. The highest cumulative release rate was observed under acidic condition (pH 5.5) mimicking the tumor microenvironment, with XAV-939 achieving 95.26 ± 3.16% and VER reaching 65.37 ± 5.23%, accompanied by significantly accelerated release kinetics at this pH. Further mechanistic analysis revealed that this pH-triggered release behavior originates from structural features shared by both drug molecules. Nitrogen-containing heterocyclic moieties within their molecular frameworks undergo enhanced protonation in acidic environments, substantially increasing molecular polarity. This structural alteration weakens hydrophobic interactions between the drugs and the polymeric micelles, destabilizing the nanocarrier and accelerating drug dissociation. Such intelligent responsiveness aligns precisely with the acidic tumor microenvironment.

3.2. Cellular Uptake and Cellular Uptake Mechanism Analysis. The intracellular concentration of therapeutic agents is a critical determinant of their pharmacological efficacy and therapeutic outcomes. Capitalizing on the intrinsic fluorescence characteristics of VER, we systematically quantified its cellular uptake through fluorescence microscopy and quantitative flow cytometry. Fluorescence microscopy images are presented in Figure 1A,B, with red fluorescence indicating the presence of VER. Following incubation with free VER and XAV-939/VER PMs, pronounced red fluorescence was observed within the cells. The fluorescence intensity increased progressively with higher drug concentrations and longer incubation periods, suggesting that drug uptake is both concentration- and time-dependent. At equivalent drug concentrations and incubation durations, the fluorescence intensity in the XAV-939/VER PMs group consistently exceeded that of the free VER group. Quantitative validation via flow cytometric analysis (Figure 1C,D and S2) corroborated the microscopic observations. These findings suggest that the formulated nanocarrier enhances drug absorption, potentially due to the distinct intracellular uptake mechanisms. Specifically, free VER is internalized via passive diffusion across the phospholipid bilayer, whereas XAV-939/VER PMs are internalized through endocytosis.

As depicted in Figure 1E, colchicine did not significantly influence the cellular uptake of XAV-939/VER PMs, while genistein and chlorpromazine significantly inhibited uptake ($p < 0.05$). Colchicine was employed to evaluate the impact of macropinocytosis on nanoparticle internalization. Genistein was utilized to assess caveolin-mediated endocytosis, and chlorpromazine was used to disrupt internalization via clathrin-coated pits. The results indicate that the cellular uptake of XAV-939/VER PMs occurs through caveolin- and clathrin-mediated endocytosis. 2-deoxy-D-glucose, a nonmetabolizable carbon source, can inhibit glycolysis at a concentration of 50 mM/L. The cellular uptake of XAV-939/VER PMs was significantly reduced following incubation with 2-deoxy-D-glucose ($p < 0.05$), indicating that the uptake process is energy-dependent and occurs via endocytosis. These findings provide mechanistic validation of our nanocarrier design strategy. The PMs not only enhance drug solubility but also alter cellular entry mechanisms, thereby overcoming key pharmacological barriers in cancer therapy.

3.3. Dark Cytotoxicity and Phototoxicity Evaluations. As illustrated in Figure 1F, free VER exhibited minimal dark toxicity at a concentration of 0.72 μg/mL, maintaining cell viability at approximately 90%. This finding aligns with the known properties of VER as a photosensitizer, which primarily exerts cytotoxic effects upon light activation. In contrast, the cell viability decreased to approximately 80% when exposed to XAV-939/VER PMs at the same concentration. This enhanced dark toxicity of XAV-939/VER PMs can be attributed to the unique physicochemical properties of the polymeric micelle formulation. The nanocarrier system facilitates increased cellular uptake, leading to higher intracellular accumulation of VER. Additionally, the presence of XAV-939 in the formulation may contribute to basal cytotoxicity by modulating cellular signaling pathways, although XAV-939 alone did not exhibit significant dark or phototoxic effects within the tested concentration range. Similarly, the phototoxicity of XAV-939/VER PMs was markedly higher than that of free VER at the identical concentration, as depicted in Figure 1G. The significantly higher cytotoxicity observed in the XAV-939/

https://doi.org/10.1021/acsami.5c04799
ACS Appl. Mater. Interfaces XXXX, XXX, XXX−XXX

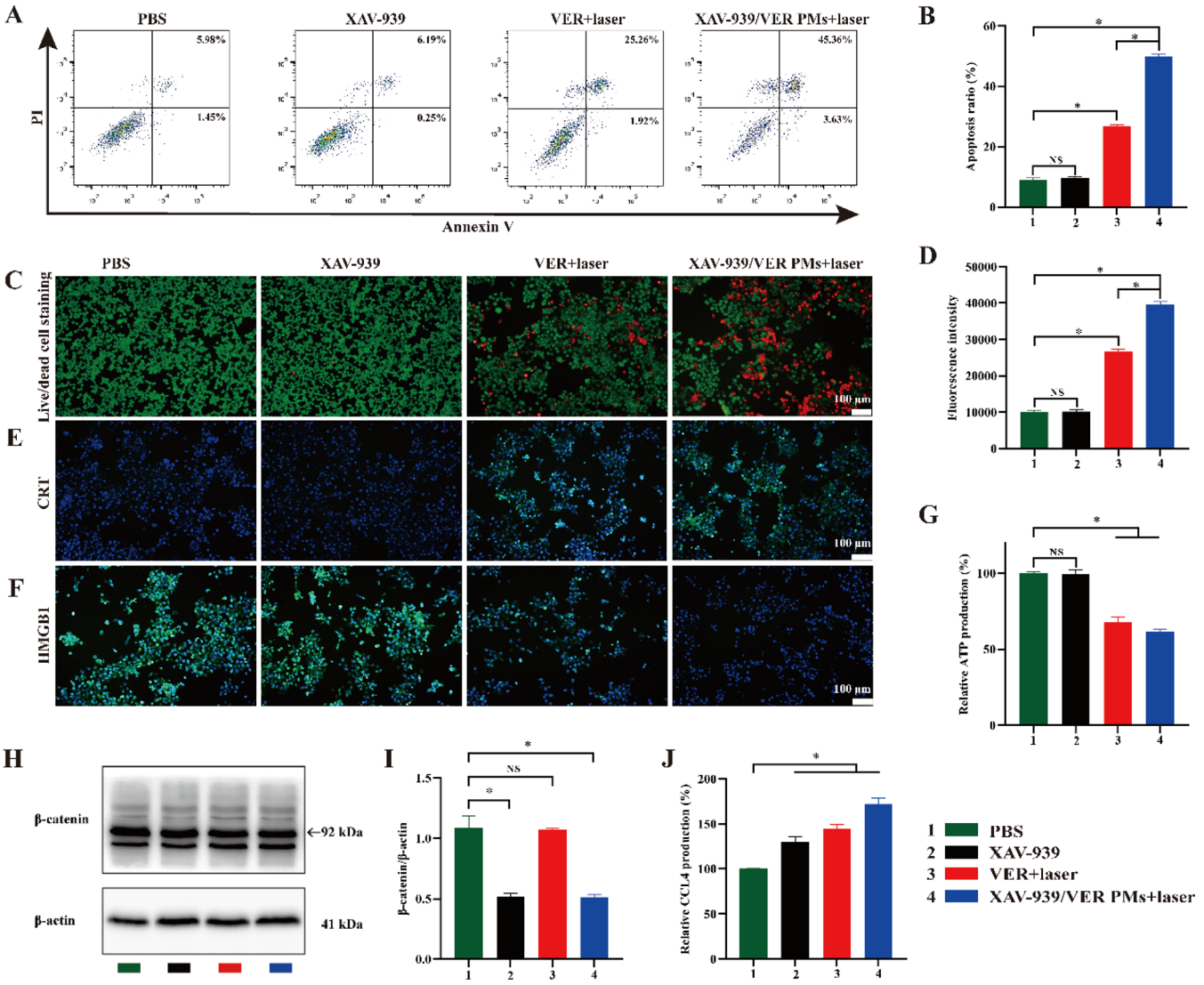

Figure 2. (A) Flow cytometry analysis of 4T1 cells after different treatments through Annexin V-APC/PI double staining. (B) Quantitative analysis of apoptosis rate. (C) Fluorescence microscopy images of live/dead cells staining after different treatments, scale bar: 100 μm. (D) Intracellular ROS generation of 4T1 cells after different treatments by flow cytometry. (E) CRT exposure and (F) intracellular HMGB1 in 4T1 cells after different treatments by fluorescence microscopy, scale bar: 100 μm. (G) Intracellular ATP content of 4T1 cells after different treatments. (H–I) β-catenin expression in 4T1 cells after different treatments. (J) CCL4 expression in 4T1 cells after different treatments.

VER PMs group underscores the importance of nanocarrier design in maximizing PDT efficacy. XAV-939 alone did not exhibit significant dark or phototoxic effects within the tested concentration range. As a selective inhibitor of the Wnt/β-catenin signaling pathway, XAV-939 primarily exerts its pharmacological effects through transcriptional regulation rather than inducing immediate cell death.

3.4. In Vitro Cell Apoptosis Detection Assay. The apoptosis data, presented in Figure 2A,B, reveal that free XAV-939 did not significantly elevate cell apoptosis compared to PBS (7.73 ± 0.42% vs 7.07 ± 0.55%, $p > 0.05$). This finding aligns with the cytotoxicity results, confirming that XAV-939 alone lacks direct cytotoxic activity at the tested concentration. Upon exposure to light, both free VER and XAV-939/VER PMs markedly enhanced apoptosis in 4T1 cells. The XAV-939/VER PMs group demonstrated a significantly higher apoptosis rate compared to the free VER group (26.65 ± 0.64% vs 49.78 ± 0.82%, $p < 0.05$). This disparity can be attributed to increased drug uptake and an augmented photodynamic effect.

3.5. Live/Dead Staining Assay. Results from the live/dead assay (Figure 2C) demonstrated that cells in the PBS and free XAV-939 groups exhibited strong green fluorescence, suggesting that XAV-939 lacked significant cytotoxicity at the tested concentration. Conversely, the free VER and XAV-939/VER PMs groups displayed both green and red fluorescence, indicating that the photosensitizer was capable of inducing cell death following laser irradiation. The proportion of red fluorescence was notably higher in the XAV-939/VER PMs group compared to the free VER group, corroborating the apoptosis and cytotoxicity data.

3.6. In Vitro ROS Measurement. Upon laser irradiation, the photosensitizer transfers absorbed photon energy to oxygen molecules, generating ROS that exert potent oxidative effects to eradicate tumor cells. An increased production of ROS results in a more pronounced photodynamic effect. Owing to the absence of photosensitive activity, free XAV-939

https://doi.org/10.1021/acsami.5c04799
ACS Appl. Mater. Interfaces XXXX, XXX, XXX−XXX

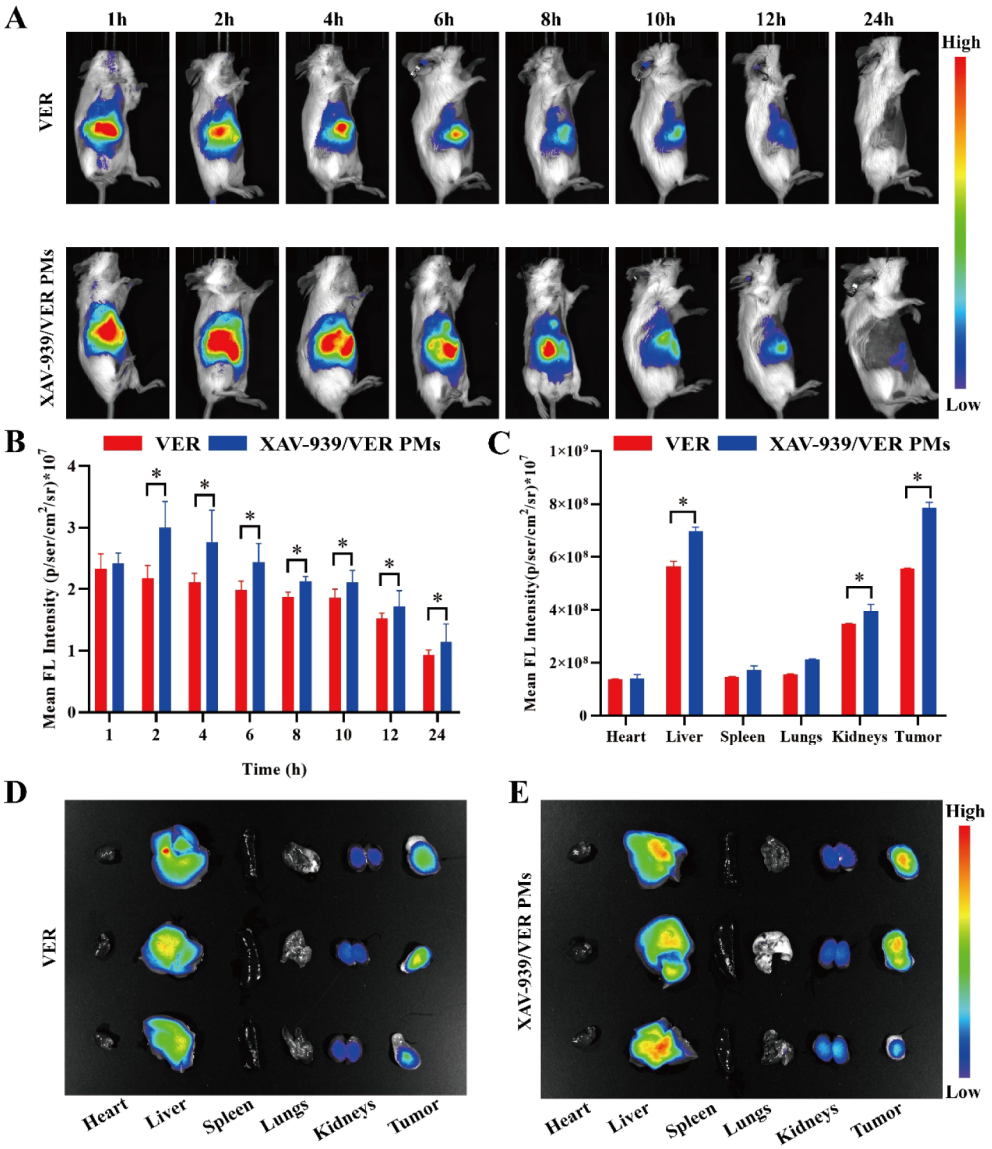

Figure 3. (A) Representative fluorescent images of mice at different time points after injection of free VER or XAV-939/VER PMs. (B) Quantification analysis of fluorescent intensity at different time points. (C-E) Ex vivo fluorescent intensity and representative fluorescent images of major organs and tumors after 24 h.

did not generate a higher level of ROS compared to the PBS group (Figure 2D). This is consistent with its known function, which is mainly focused on modulating the intracellular signaling cascade rather than participating in photochemical reactions. Conversely, both the free VER and XAV-939/VER PMs groups exhibited substantial ROS production following laser irradiation. Notably, ROS generation in the XAV-939/VER PMs group was significantly greater than that in the free VER group, potentially accounting for the markedly enhanced phototoxicity of XAV-939/VER PMs relative to free VER. This elevated ROS production may be attributed to increased drug uptake.

3.7. In Vitro Immunogenic Cell Death Assay. Previous studies have extensively demonstrated that PDT can induce ICD through the potent oxidative effects of ROS. This induction process is of great significance as it can effectively trigger an antitumor immune response.[29] ICD is characterized by the translocation of calreticulin (CRT) from the endoplasmic reticulum to the cell membrane surface, along with the extracellular release of high-mobility group box-1 (HMGB1) and adenosine triphosphate (ATP).[30] During ICD, CRT exposed on the cell membrane surface acts as an "eat me" signal, facilitating the phagocytosis of dead or dying tumor cells by DCs or their progenitors, and providing abundant antigens to stimulate DC maturation and functional activation.[31] The extracellular release of HMGB1 and ATP can activate specific signaling pathways, thereby stimulating the immune system.[32] These combined effects of CRT, HMGB1, and ATP release during ICD create a pro-inflammatory and immunostimulatory environment that is conducive to mounting an antitumor immune response.

Figure 2E demonstrates that the level of CRT exposure was minimal in the group treated with free XAV-939, suggesting that XAV-939 alone does not induce ICD in tumor cells. XAV-939, as a small-molecule inhibitor targeting the Wnt/β-catenin signaling pathway, may not directly affect the molecular events associated with ICD induction. However, following laser irradiation, both the free VER and XAV-939/VER PMs groups

https://doi.org/10.1021/acsami.5c04799
ACS Appl. Mater. Interfaces XXXX, XXX, XXX−XXX

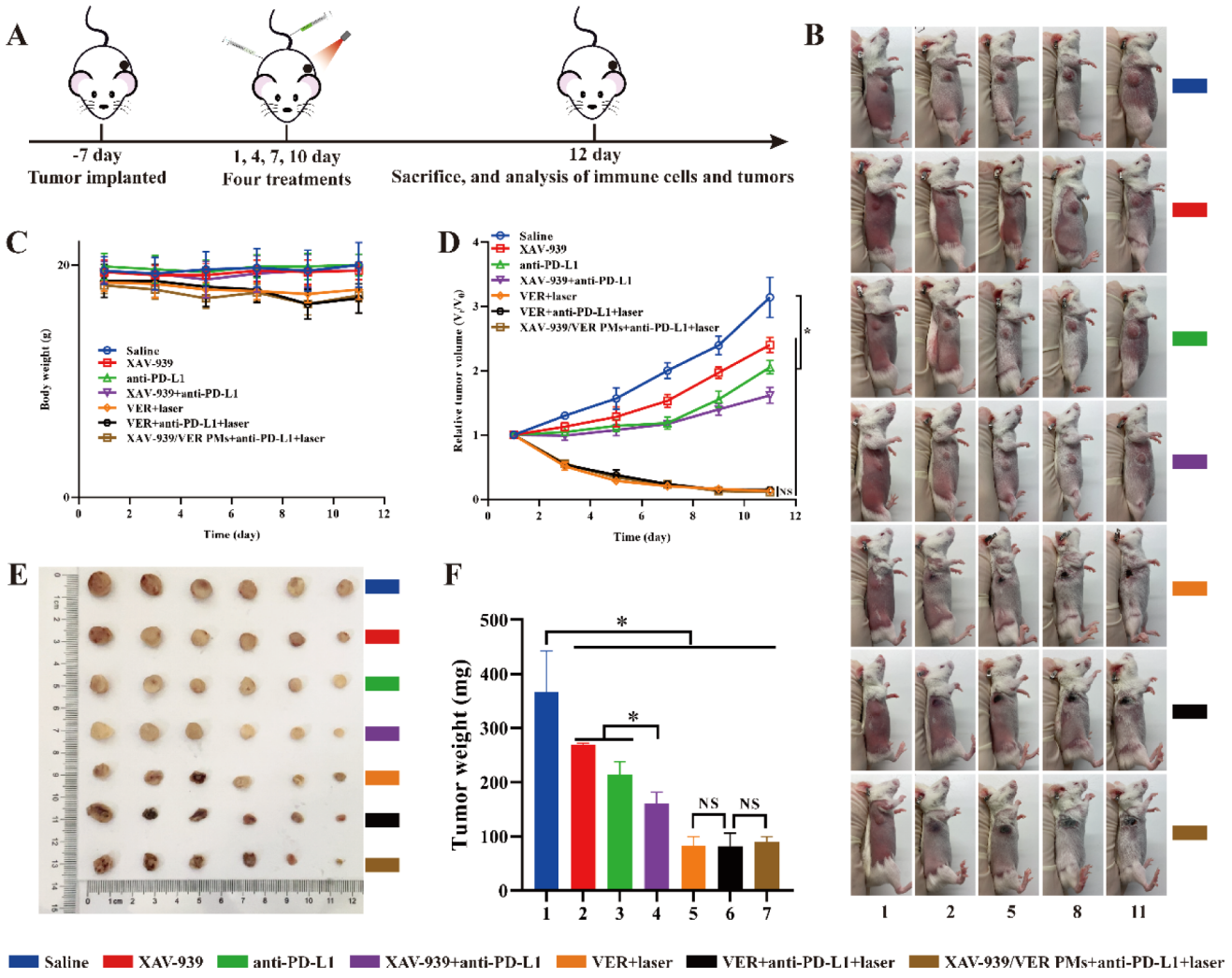

Figure 4. (A) Schematic illustration of the animal experimental design for primary tumor. (B) Representative images of 4T1 tumor-bearing mice following different treatments on days 1, 2, 5, 8, and 11. (C) Mice's body weight changes and (D) primary tumor volume changes in different treatment groups. (E) Representative images and (F) weights of ex vivo tumor tissues in different groups on the 12th day.

exhibited strong green fluorescence, which is a clear indication of substantial CRT exposure on the cell surface. Notably, the XAV-939/VER PMs group displayed a higher level of CRT exposure compared to the free VER group. During ICD, tumor cells release significant amounts of HMGB1 and ATP extracellularly, resulting in reduced intracellular levels of these molecules. The results indicate no significant difference in intracellular levels of HMGB1 and ATP between the PBS- and XAV-939-treated groups (Figure 2F, G). This further supports the finding that XAV-939 alone does not induce ICD. Conversely, a significant reduction in intracellular levels of HMGB1 and ATP was observed in both the free VER and XAV-939/VER PMs groups, with the most substantial decrease occurring in the XAV-939/VER PMs group. The findings indicate that the polymer micelle carrier indeed facilitated enhanced uptake of VER. The increased intracellular concentration of VER can enhance the production of ROS during PDT, and the elevated ROS levels can then more effectively induce ICD. The induction of ICD provides a solid foundation for antitumor immunotherapy. By triggering ICD, PDT can transform the TME from an immunosuppressive state to an immunostimulatory one. This transformation can potentially enhance the efficacy of other antitumor therapies, such as ICIs, by promoting the activation and infiltration of immune cells into the tumor tissue.

3.8. β-Catenin and CCL4 Detection. As illustrated in Figure 2H,I, both free XAV-939 and XAV-939/VER PMs were effective in reducing β-catenin expression. No significant difference in β-catenin expression was observed between the free VER and PBS groups, suggesting that VER-mediated PDT does not influence β-catenin expression. Free XAV-939, free VER, and XAV-939/VER PMs significantly enhanced CCL4 secretion by tumor cells (Figure 2J). Interestingly, PDT can also facilitate chemokine release, which may be a result of the stress response induced by PDT in tumor cells. XAV-939 can inhibit the Wnt/β-catenin signaling pathway, which as previously mentioned, is associated with reduced CCL4 secretion. These findings imply that combining PDT with the downregulation of the Wnt/β-catenin signaling pathway may synergistically enhance the immunosuppressive TME. By combining the two approaches, on one hand, PDT can directly damage tumor cells and also induce the release of chemokines like CCL4. On the other hand, inhibiting the Wnt/β-catenin signaling pathway with XAV-939 can further enhance CCL4 secretion and reverse the immunosuppressive effects of β-

https://doi.org/10.1021/acsami.5c04799
ACS Appl. Mater. Interfaces XXXX, XXX, XXX−XXX

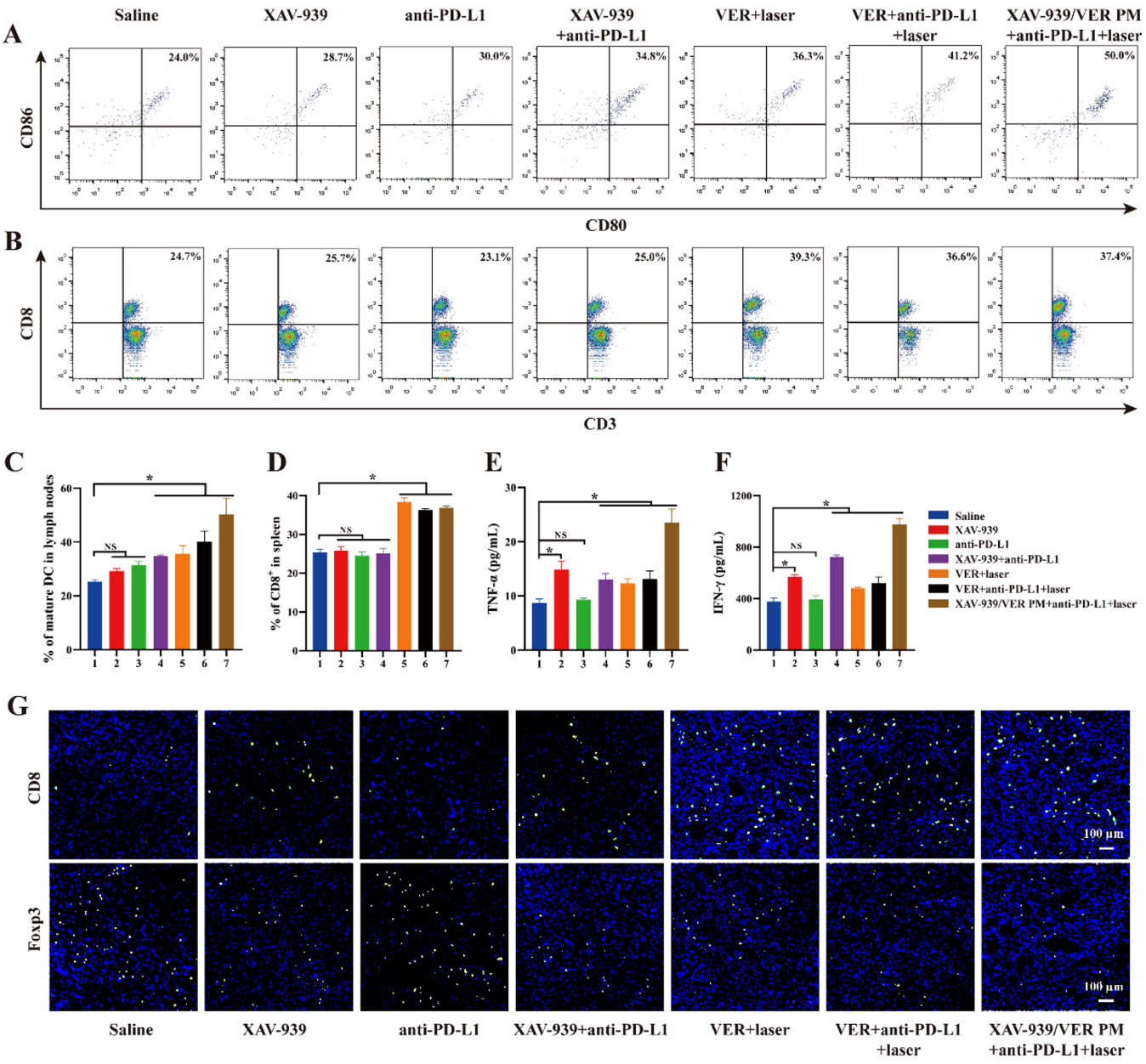

Figure 5. (A) Representative flow cytometry plot and (C) quantitative analysis of mature DCs in lymph nodes. (B) Representative flow cytometry plot and (D) quantitative analysis of CD8+T cells in the spleen. The expression levels of TNF-α (E) and IFN-γ (F) in different groups. (G) Representative immunofluorescence images of CD8+ and Foxp3+ cells in primary tumor tissues from different groups, scale bar: 100 μm.

catenin, potentially leading to a more effective antitumor immune response.

3.9. In Vivo Tumor Imaging and Biodistribution. The effective accumulation of nanoparticles within the tumor region is critical for therapeutic efficacy. To accurately determine the optimal timing for laser irradiation following the intravenous administration of XAV-939/VER PMs in tumor-bearing mice and to comprehensively elucidate the in vivo biodistribution of XAV-939/VER PMs, a small animal in vivo imaging system was utilized in this study. As illustrated in Figure 3A,B, distinct fluorescence signals were detected in the tumor region as early as 1 h postintravenous injection of either free VER or XAV-939/VER PMs. In the free VER group, the fluorescence intensity demonstrated a gradual decline over time. This could be attributed to the relatively rapid clearance of free VER from the bloodstream and its limited ability to accumulate specifically in the tumor tissue. In contrast, following the administration of XAV-939/VER PMs, the fluorescence intensity reached its peak between 2 to 4 h. This peak indicates that the XAV-939/VER PMs were gradually accumulating in the tumor tissue during this period. Subsequently, the fluorescence intensity decreased, which was a normal pattern as the nanoparticles were either metabolized or cleared from the body. Notably, the fluorescence intensity of XAV-939/VER PMs surpassed that of free VER after 2 h. This significant difference implies that the polymer micelle carrier plays a crucial role in enhancing drug accumulation in tumors. The most likely mechanism underlying this enhanced accumulation is the EPR effect. Consequently, based on these findings, a 2-h postadministration interval is recommended as the optimal time for laser exposure in subsequent in vivo pharmacodynamic studies. At this time point, the highest

https://doi.org/10.1021/acsami.5c04799
ACS Appl. Mater. Interfaces XXXX, XXX, XXX−XXX

concentration of XAV-939/VER PMs is present in the tumor tissue, maximizing the potential for PDT to exert its antitumor effects.

After 24 h, tumors and major organs were carefully excised for fluorescence intensity measurement. As illustrated in Figure 3C−E, fluorescence signals were predominantly localized in tumor tissues and organs with well-developed reticuloendothelial systems, such as the liver and kidneys. This indicates that XAV − 939/VER PMs can persist in tumor tissue for extended durations, which is beneficial for sustained antitumor effects. Additionally, it suggests that the liver is the main site of metabolism for these nanoparticles. The fluorescence intensity of XAV-939/VER PMs in tumor tissues and the liver was significantly greater than that of free VER (Figure 3C). The DSPE-mPEG2000 component, which incorporates a PEG structure, also plays a pivotal role in this process. The PEG structure on the surface of the nanoparticles enhances their prolonged circulation properties. This, in turn, improves their EPR performance, as more nanoparticles have the opportunity to reach the tumor tissue through the leaky tumor blood vessels.

3.10. Evaluation of Primary Antitumor Effects. To assess the efficacy of the combination therapy, subcutaneous 4T1 tumor-bearing mice, characterized by low immune response and poor immunogenicity, were utilized (Figure 4). As depicted in Figure 4C, mice subjected to laser irradiation exhibited some degree of weight loss, while the body weight of mice in other groups remained relatively stable. During PDT treatment process, the limbs of the mice were immobilized, and PDT can induce inflammation at the site of light exposure. These factors may have influenced the condition of the mice, subsequently affecting their food intake and body weight. According to Figure 4D, there was a significant reduction in tumor volume in the laser irradiation groups, with minimal differences observed between these groups. This indicates that PDT demonstrated a rapid and substantial effect in decreasing tumor volume. In these groups, it is highly likely that PDT played a predominant role in tumor volume reduction. The strong antitumor effect of PDT might have overshadowed the potential contributions of XAV-939 and anti-PD-L1. Separately, the tumor growth rate was significantly reduced in the XAV-939 and anti-PD-L1 groups compared to the saline group ($p < 0.05$). This clearly shows that both XAV-939 and anti-PD-L1 can independently inhibit tumor growth. More importantly, when XAV-939 was combined with anti-PD-L1 (in the XAV-939 plus anti-PD-L1 group), a further reduction in the tumor growth rate was achieved. This significant finding indicates that the downregulation of the Wnt/β-catenin signaling pathway, when combined with ICIs, can synergistically inhibit tumor growth. The underlying mechanism may involve the restoration of the immune response by blocking the immunosuppressive Wnt/β-catenin pathway and simultaneously unleashing the antitumor activity of T cells through the blockade of PD-L1. Figure 4E,F further illustrate and corroborate the findings presented in Figure 4D. All treatment groups significantly inhibited tumor growth compared to the saline group. The combination of different therapeutic approaches, such as PDT, XAV-939, and anti-PD-L1, holds great promise for improving cancer treatment outcomes.

3.11. In Vivo Immune Response and Cytokines Evaluation. Researches have been conducted to elucidate the mechanisms underlying this combined therapeutic strategy. This strategy holds great promise not only in understanding the complex interplay between different treatment modalities but also in evaluating its potential to transform tumors from a "cold" state to a "hot" state. DCs are widely acknowledged as the most potent professional APCs within the mammalian body. DCs maturation is a prerequisite for their ability to efficiently present tumor antigens to T cells and activate them. This initial activation of T cells by DCs sets in motion a cascade of immune events that are essential for mounting an effective antitumor immune response.[33]

Figure 5A,C demonstrate that the proportion of mature DCs increased in the XAV-939 and anti-PD-L1 groups compared to the saline group, although these differences were not statistically significant ($p > 0.05$). This lack of significance could be attributed to several factors, such as the relatively short-term nature of the treatment, the specific dosing regimens used, or the inherent variability in the immune response of individual animals. However, a statistically significant increase was observed when the treatments were combined (XAV-939 plus anti-PD-L1). This finding strongly suggests a potential synergistic effect between the downregulation of the Wnt/β-catenin signaling pathway and the blockade of the PD-L1 immune checkpoint. In the laser irradiation groups, a significant increase in the proportion of mature DCs was also noted ($p < 0.05$), further validating the prominent role of PDT in inducing antitumor immune responses. Notably, the XAV-939/VER PMs plus anti-PD-L1 plus laser treatment group exhibited the highest percentage of mature DCs. The findings suggest that the integration of PDT with the downregulation of the Wnt/β-catenin signaling pathway and immune checkpoint blockade can significantly enhance DCs maturation.

Cytotoxic T lymphocytes (CD8+ T cells), commonly known as killer T cells, play a crucial role in the body's antitumor immunity by targeting and eliminating tumor cells through the recognition of specific antigens.[34] Conversely, regulatory T cells (Tregs), a subset of T cells marked by the expression of Foxp3, CD4, and CD25, can attenuate the immune response. This attenuation of the immune response by Tregs can potentially lead to tumor immune evasion, where tumors are able to avoid detection and destruction by the immune system.[35]

As illustrated in Figure 5B,D, treatments with XAV-939, anti-PD-L1, and their combination did not result in a significant increase in the proportion of CD8+ T lymphocytes in the spleen compared to the saline control group. However, a more detailed analysis of the tumor tissue, as depicted in Figure 5G, revealed an interesting phenomenon. Both XAV-939 alone and in combination with anti-PD-L1 significantly enhanced the proportion of CD8+ T lymphocytes while concomitantly reducing the proportion of Tregs within the tumor tissue. XAV-939 may disrupt the immunosuppressive signals within the TME. The downregulation of the Wnt/β-catenin signaling pathway could potentially interfere with the recruitment and function of Tregs, while also promoting the activation and infiltration of CD8+ T cells. Notably, the PDT treatment groups demonstrated a more pronounced increase in the proportion of CD8+ T lymphocytes in both the spleen and tumor tissue, alongside a more significant reduction in Tregs within the tumor tissue, compared to other treatment groups. These findings clearly indicate that PDT is more efficacious in modulating the immunosuppressive TME.

TNF-α and IFN-γ are two pivotal pro-inflammatory cytokines that play multifaceted and crucial roles in immune-

https://doi.org/10.1021/acsami.5c04799
ACS Appl. Mater. Interfaces XXXX, XXX, XXX−XXX

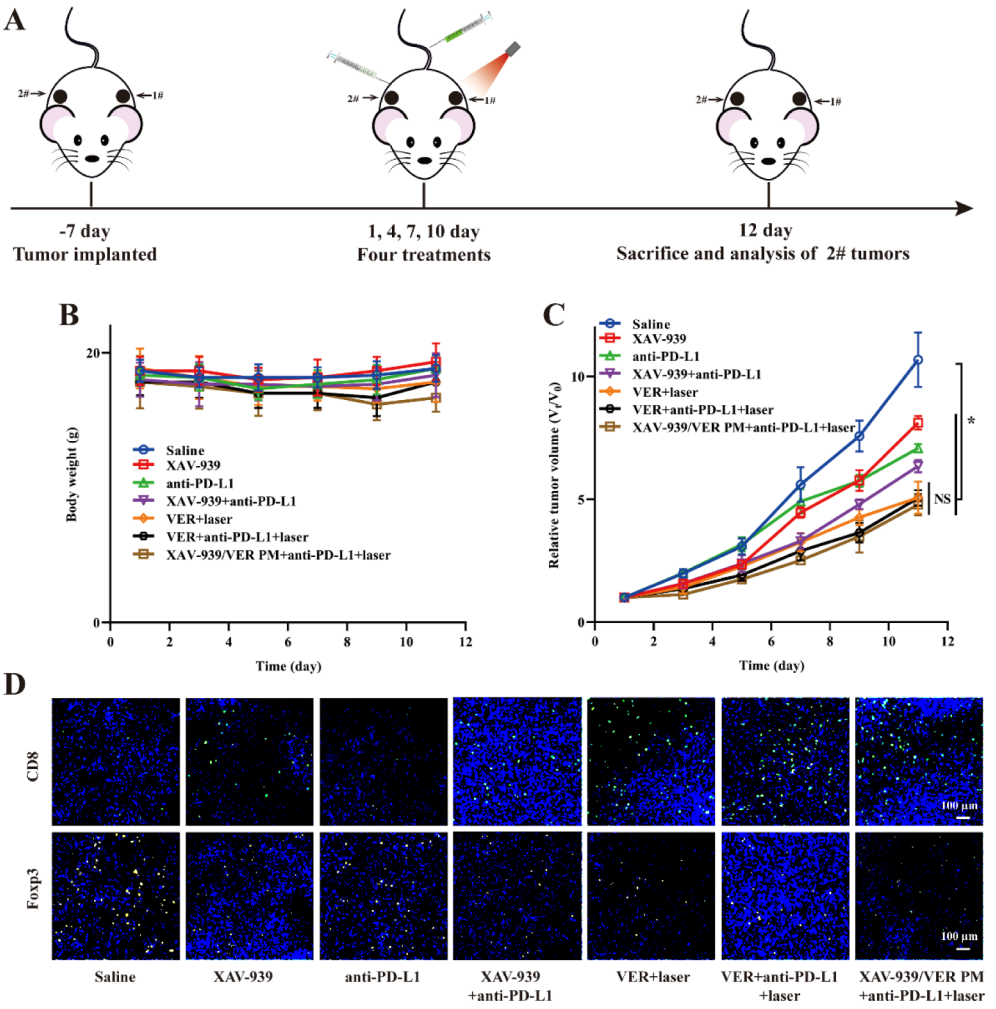

Figure 6. (A) Schematic illustration of the animal experimental design for distal tumor. (B) Mice's body weight changes and (C) distal tumor volume changes in different treatment groups. (D) Representative immunofluorescence images of CD8+ and Foxp3+ cells in distal tumor tissues from different groups, scale bar: 100 μm.

inflammatory responses.[36] TNF-α is a cytokine that can be produced by a variety of immune cells, including T lymphocytes, macrophages, and natural killer cells. It has a wide range of functions, with both immunostimulatory and immunoregulatory properties. IFN-γ, mainly produced by activated T lymphocytes and natural killer cells, also has a dual-function nature. It is a powerful immunostimulant, capable of enhancing the antigen-presenting function of DCs and increasing the ability of macrophages to kill intracellular pathogens and tumor cells.

The serum levels of TNF-α and IFN-γ were quantified using an ELISA kit, with the results presented in Figure 5E,F. It is notable that the expression levels of TNF-α and IFN-γ in the anti-PD-L1 group did not show significant differences compared to the saline group. In contrast, all other experimental groups demonstrated a significant upregulation in the expression levels of TNF-α and IFN-γ. By downregulating the Wnt/β-catenin signaling pathway, XAV-939 may disrupt the immunosuppressive signals, leading to enhanced immune cell activation and cytokine production. The PDT process can lead to the release of DAMPs from tumor cells, which can activate immune cells and promote the secretion of cytokines. The combination of PDT, downregulation of the Wnt/β-catenin signaling pathway, and anti-PD-L1 may have a synergistic effect, with the XAV-939/VER PMs plus anti-PD-L1 plus laser group exhibiting the highest expression levels.

3.12. Evaluation of Distal Antitumor Effects. By activating immune cells, immunotherapy has the potential to suppress distant tumors, which are often a major concern in cancer progression as they can lead to metastasis, and also prevent tumor recurrence, a significant challenge in achieving long-term cancer remission. In this study, a distal tumor model was established to assess the inhibitory effects of the innovative photodynamic-downregulating Wnt/β-catenin signaling-immunotherapy strategy on multiple tumors, mimicking the complex in vivo scenario where cancer cells may spread to distant sites. As depicted in Figure 6B, the body weight of mice in the laser irradiation groups decreased, whereas the body weight of mice in other groups remained relatively stable, corroborating the findings presented in the Evaluation of Primary Anti-Tumor Effects section. Figure 6C illustrates that the groups treated with XAV-939, anti-PD-L1, and XAV-939 plus anti-PD-L1 exhibited a statistically significant reduction in distant tumor growth compared to the saline group ($p < 0.05$). The combination of XAV-939 and anti-PD-L1 may have a synergistic effect, further enhancing the antitumor immune response. Notably, the groups subjected to laser irradiation demonstrated a more pronounced inhibitory effect on distal

https://doi.org/10.1021/acsami.5c04799
ACS Appl. Mater. Interfaces XXXX, XXX, XXX−XXX

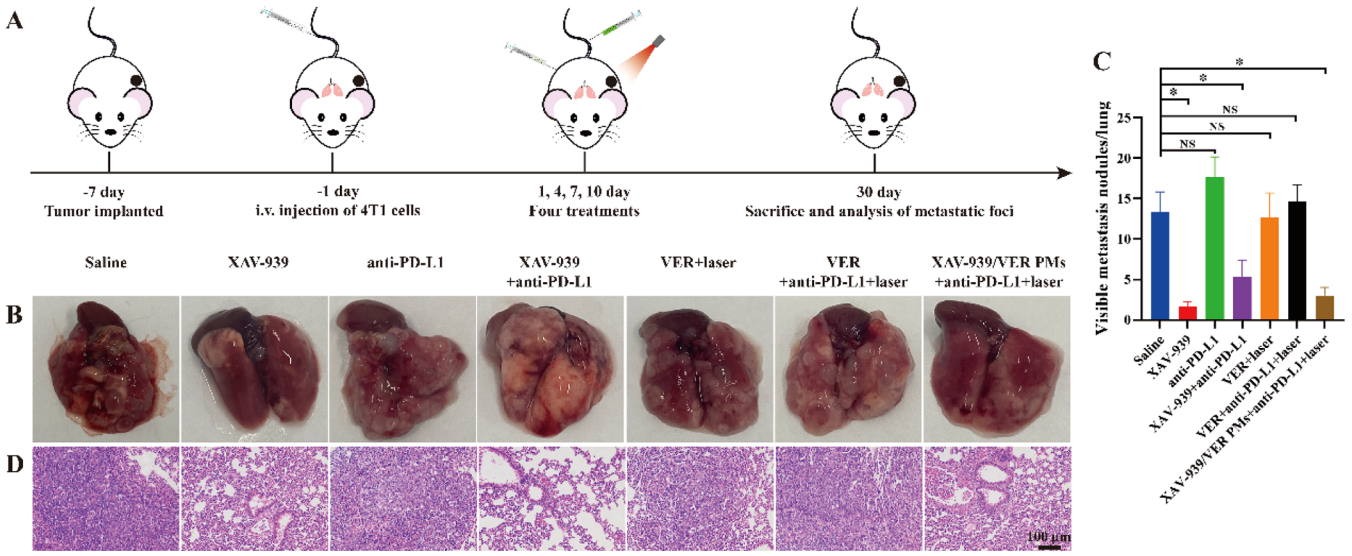

Figure 7. (A) Schematic illustration of the animal experimental design for pulmonary metastasis study. Representative images of (B) lung metastasis, (C) corresponding quantitative results of lung nodules, and (D) representative images of H&E-stained sections of lung tissues, scale bar: 100 μm.

tumors. This could be potentially due to enhanced activation of the host immune system.

To evaluate the degree of immune system activation and investigate the underlying mechanisms of the combined treatment strategy in suppressing distal tumors, the infiltration of CD8+ T lymphocytes and Tregs in distal tumors was examined using immunofluorescence (Figure 6D). Relative to the saline group, both the XAV-939 and XAV-939 plus anti-PD-L1 groups showed increased infiltration of CD8+ T lymphocytes and a reduction in Foxp3+ (Tregs) expression in distant tumor tissues. The increase in CD8+ T cell infiltration indicates enhanced antitumor immune activity, while the reduction in Tregs suggests a decrease in immunosuppression. The laser irradiation groups outperformed the XAV-939 and XAV-939 plus anti-PD-L1 groups in terms of CD8+ T cell infiltration and Treg reduction. This difference may account for their superior inhibitory effects on distant tumors. The combination of PDT with the downregulation of the Wnt/β-catenin signaling pathway and immune checkpoint blockade may lead to a more comprehensive and potent activation of the immune system, creating a more favorable immune environment for the suppression of distant tumors.

3.13. Evaluation of Antipulmonary Metastatic Effects.

Cancer cell metastasis remains a primary cause of chemotherapy failure and cancer-related mortality in breast cancer patients. Once metastasized, these cancer cells can form new tumor nodules, which are often more difficult to treat compared to the primary tumor. In this study, a 4T1 lung metastasis model was established to evaluate the effectiveness of the photodynamic-downregulating Wnt/β-catenin signaling-immunotherapy strategy in a preclinical setting that closely mimics the in vivo situation of breast cancer metastasis.

Figure 7B,C illustrate that the saline-treated group exhibited numerous tumor nodules within the lung tissue, corroborating the highly metastatic nature of 4T1 breast cancer. The number of tumor nodules in the anti-PD-L1, VER plus laser, and VER plus anti-PD-L1 plus laser groups did not show a statistically significant reduction compared to the saline group ($p > 0.05$), suggesting that anti-PD-L1 and VER-mediated PDT were ineffective in inhibiting lung metastasis. Conversely, a strikingly different outcome was observed in the groups treated with XAV-939, XAV-939 plus anti-PD-L1, and XAV-939/VER PMs plus anti-PD-L1 plus laser. These groups demonstrated a significant reduction in tumor nodules ($p < 0.05$). The histological examination of H&E-stained lung sections (Figure 7D) further revealed that only a few tumor cells were observable in these groups. XAV-939 appears to exert a substantial inhibitory effect on lung metastasis. The Wnt/β-catenin signaling pathway has been previously implicated in various aspects of cancer progression, including cell adhesion, migration, and invasion. In the context of metastasis, dysregulation of this pathway can promote the detachment of cancer cells from the primary tumor, their intravasation into the bloodstream or lymphatics, and subsequent extravasation and colonization at distant sites. By downregulating the Wnt/β-catenin signaling pathway, XAV-939 may disrupt these processes, thereby inhibiting tumor lung metastasis.

These findings suggest a strong and potentially causal association between the Wnt/β-catenin signaling pathway and tumor lung metastasis. The remarkable efficacy of XAV-939 in suppressing tumor lung metastasis holds significant clinical potential, especially for TNBC. TNBC is a particularly aggressive subtype of breast cancer characterized by high invasiveness and metastatic propensity. The results of this study indicate that targeting the Wnt/β-catenin signaling pathway with XAV-939, either alone or in combination with other therapies, could potentially offer a new and effective treatment approach for TNBC patients, reducing the incidence of lung metastasis and improving overall survival.

The translational value of this strategy is highlighted by its potential to address critical challenges in TNBC treatment. First, the combination of PDT with Wnt/β-catenin inhibition (XAV-939) and anti-PD-L1 demonstrated dual control over primary tumor growth and metastasis, a critical unmet need for TNBC patients who often develop resistance to monotherapies. Notably, the synergistic reduction in Tregs and increased CD8+ T cell infiltration suggest that rewiring the immunosuppressive TME could sensitize "cold" TNBC tumors to checkpoint inhibitors, a key hurdle in current immunotherapy. Second, the significant suppression of lung metastasis by

https://doi.org/10.1021/acsami.5c04799
ACS Appl. Mater. Interfaces XXXX, XXX, XXX−XXX

XAV-939 underscores its clinical relevance, as metastatic TNBC has a dismal 5-year survival rate. Finally, the activation of systemic immunity (distal tumor suppression) aligns with emerging paradigms in immuno-oncology, where local therapies are repurposed to generate abscopal effects. These findings position this strategy as a multimodal solution for TNBC's triple threat: immunosuppression, metastasis, and therapeutic resistance.

4. CONCLUSION

This study presents a multimodal nanotherapeutic strategy that synergizes photodynamic therapy with Wnt/β-catenin pathway inhibition to rewire TNBC's immunosuppressive TME. The self-assembled polymeric platform achieves codelivery of dual payloads, overcoming solubility limitations and enhancing tumor accumulation through the EPR effect. By simultaneously inducing ICD and disrupting β-catenin-mediated immune evasion, the nanosystem effectively converts "cold" tumors into environments permissive to ICIs. Key findings include enhanced drug delivery, improved immune cell infiltration, and synergistic antitumor activity in primary, distant, and metastatic disease models. These results highlight the promise of targeted TME reprogramming as a strategy to overcome TNBC's recalcitrance to immunotherapy. However, several limitations and future directions must be acknowledged. The long-term safety profile requires validation through extended toxicity studies in animal models. The translational relevance of findings could be strengthened by incorporating patient-derived xenografts or organoid models, which better recapitulate the genetic heterogeneity of human TNBC compared to the 4T1 cell line-based system used here. Looking forward, engineering stimuli-responsive nanocarriers for spatiotemporal control of drug release, integrating novel immune agonists (e.g., STING or OX40 inhibitors), and investigating gut microbiota-mediated modulation of therapeutic responses represent promising avenues to amplify antitumor immunity. This multimodal paradigm not only addresses TNBC's triad of challenges but also opens new horizons for treating other aggressive cancers characterized by dysregulated Wnt signaling and immune exclusion.

■ ASSOCIATED CONTENT

Data Availability Statement

Data will be made available on request.

Supporting Information

The Supporting Information is available free of charge at https://pubs.acs.org/doi/10.1021/acsami.5c04799.

Detailed experimental procedures; representative TEM image of the XAV-939/VER PMs; size distribution of the XAV-939/VER PMs; zeta potential of the XAV-939/VER PMs; UV−vis absorption spectra and fluorescence spectra of XAV-939, VER, XAV-939/VER PMs, DSPE-mPEG 2000, and cholesterol; hydrodynamic diameter changes of XAV-939/VER PMs after incubation with Tween-20, SDS, and urea at varying concentrations for 24 h; laser irradiation (0.3 W/cm^2, 15 min) stability of VER and XAV-939/VER PMs; changes of the hydrodynamic diameter and the polydispersity index of the XAV-939/VER PMs in PBS containing 10% FBS over 5 days; cumulative release profiles of XAV-939 and VER from XAV-939/VER PMs under different conditions; cellular uptake of free VER and XAV-939/VER PMs by 4T1 cells at different concentrations of VER (0.18, 0.36, 0.72 μg/mL) by flow cytometry; cellular uptake of free VER and XAV-939/VER PMs by 4T1 cells at 30, 60, and 120 min by flow cytometry(PDF)

■ AUTHOR INFORMATION

Corresponding Authors

Jia Yan − *Department of Pharmacy, 900th Hospital of PLA Joint Logistic Support Force, Fuzhou 350025, PR China*; Phone: +86-0591-2285-9963; Email: 25831145@qq.com

Xin Zhou − *Department of Pharmacy, 900th Hospital of PLA Joint Logistic Support Force, Fuzhou 350025, PR China*; Phone: +86-0591-2285-9169; Email: fzzyjg@163.com

Authors

Lingjun Zeng − *Department of Pharmacy, 900th Hospital of PLA Joint Logistic Support Force, Fuzhou 350025, PR China*; orcid.org/0009-0001-7517-4991

Kaiqin You − *Department of Pharmacy, 900th Hospital of PLA Joint Logistic Support Force, Fuzhou 350025, PR China*

Mingjian Lu − *Department of Pharmacy, Yongding District Hospital of Longyan City, Longyan 364100, PR China*

Xiaomu Hu − *Department of Pharmacy, 900th Hospital of PLA Joint Logistic Support Force, Fuzhou 350025, PR China*

Changqing Zheng − *Department of Pharmacy, 900th Hospital of PLA Joint Logistic Support Force, Fuzhou 350025, PR China*

Lingyan Yao − *Department of Pharmacy, 900th Hospital of PLA Joint Logistic Support Force, Fuzhou 350025, PR China*

Bingkun Kang − *Department of Pharmacy, 900th Hospital of PLA Joint Logistic Support Force, Fuzhou 350025, PR China*

Shuang Lin − *Department of Pharmacy, 900th Hospital of PLA Joint Logistic Support Force, Fuzhou 350025, PR China*

Xiaoliang Deng − *Department of Pharmacy, 900th Hospital of PLA Joint Logistic Support Force, Fuzhou 350025, PR China*

Complete contact information is available at: https://pubs.acs.org/10.1021/acsami.5c04799

Author Contributions

[§]L.Z. and K.Y. contributed equally to this article and contributed to the validation, software, writing − original draft, writing − review and editing, and investigation. M.L., X.H., C.Z., L.Y., B.K., S.L., and X.D. contributed to the investigation of the article. J.Y. contributed to the conceptualization and supervision. X.Z. contributed to the conceptualization, supervision, funding acquisition, and project administration.

Funding

This work was supported by the Joint Fund for Program of Science Innovation of Fujian Province, China [grant numbers: 2024Y9645, 2022J011092].

Notes

The authors declare no competing financial interest.

■ ACKNOWLEDGMENTS

We appreciate the Public Technology Service Center of Fujian Medical University for technical assistance and Phadcalc (www.phadcalc.com) for the molecular docking simulation.

REFERENCES

(1) Bray, F.; Laversanne, M.; Sung, H.; Ferlay, J.; Siegel, R. L.; Soerjomataram, I.; Jemal, A. Global cancer statistics 2022: GLOBOCAN estimates of incidence and mortality worldwide for 36 cancers in 185 countries. *Ca-Cancer J. Clin.* **2024**, *74*, 229−263.

(2) Bianchini, G.; De Angelis, C.; Licata, L.; Gianni, L. Treatment landscape of triple-negative breast cancer - expanded options, evolving needs. *Nat. Rev. Clin. Oncol.* **2022**, *19*, 91−113.

(3) Derakhshan, F.; Reis-Filho, J. S. Pathogenesis of Triple-Negative Breast Cancer. *Annu. Rev. Pathol.: mech. Dis.* **2022**, *17*, 181−204.

(4) O'Shaughnessy, J.; Osborne, C.; Pippen, J. E.; Yoffe, M.; Patt, D.; Rocha, C.; Koo, I. C.; Sherman, B. M.; Bradley, C. Iniparib plus chemotherapy in metastatic triple-negative breast cancer. *N. Engl. J. Med.* **2011**, *364*, 205−214.

(5) Bianchini, G.; Balko, J. M.; Mayer, I. A.; Sanders, M. E.; Gianni, L. Triple-negative breast cancer: challenges and opportunities of a heterogeneous disease. *Nat. Rev. Clin. Oncol.* **2016**, *13*, 674−690.

(6) Miles, D.; Gligorov, J.; André, F.; Cameron, D.; Schneeweiss, A.; Barrios, C.; Xu, B.; Wardley, A.; Kaen, D.; Andrade, L.; et al. Primary results from IMpassion131, a double-blind, placebo-controlled, randomised phase III trial of first-line paclitaxel with or without atezolizumab for unresectable locally advanced/metastatic triple-negative breast cancer. *Annals Oncol.* **2021**, *32*, 994−1004.

(7) Enokida, T.; Moreira, A.; Bhardwaj, N. Vaccines for immunoprevention of cancer. *J. Clin. Invest.* **2021**, *131* (9), No. e146956.

(8) Wang, D. Y.; Liu, J. W.; Duan, J.; Ma, Y. R.; Gao, H.; Zhang, Z. Z.; Liu, J. J.; Shi, J. J.; Zhang, K. X. Photocontrolled Spatiotemporal Delivery of DNA Immunomodulators for Enhancing Membrane-Targeted Tumor Photodynamic Immunotherapy. *ACS Appl. Mater. Interfaces* **2022**, *14*, 44183−44198.

(9) Liao, L.; Liu, Y. F.; Li, X. H.; Jiang, Z. W.; Jiang, Z. J.; Yao, J. X. Dual-Regulated Biomimetic Nanocomposites for Promoted Tumor Photodynamic Immunotherapy. *ACS Appl. Mater. Interfaces* **2025**, *17*, 20919−20931.

(10) Cen, Y.; Li, X. X.; Wang, M.; Chen, Y.; Ou, X. C.; Yu, B. X.; Chen, X. Y.; Wang, Y. Q.; Guo, N.; Li, S. Y. Chimeric Peptide Functionalized Immunostimulant to Orchestrate Photodynamic Immunotherapeutic Effect by PD-L1 Deglycosylation and CD47 Inhibition. *ACS Appl. Mater. Interfaces* **2025**, *17*, 7539−7552.

(11) Huang, W.; Shi, S. J.; Lv, H. R.; Ju, Z. Y.; Liu, Q. H.; Chen, T. F. Tellurium-driven maple leaf-shaped manganese nanotherapeutics reshape tumor microenvironment via chemical transition in situ to achieve highly efficient radioimmunotherapy of triple negative breast cancer. *Bioact. Mater.* **2023**, *27*, 560−573.

(12) Wu, F.; Feng, X. Q.; Gao, W. H.; Zeng, L. J.; Xu, B. B.; Chen, Z. Z.; Zheng, C. Q.; Hu, X. M.; Xu, S. Y.; Song, H. T.; Zhou, X.; Liu, Z. H. Engineering a Self-Delivery Nanoplatform for Chemo-Photodynamic-Immune Synergistic Therapies against Aggressive Melanoma. *ACS Appl. Mater. Interfaces* **2025**, *17*, 11634−11652.

(13) Ji, B.; Wei, M. J.; Yang, B. Recent advances in nanomedicines for photodynamic 942 therapy (PDT)-driven cancer immunotherapy. *Theranostics* **2022**, *12*, 434−458.

(14) Sun, F.; Zhu, Q.; Li, T.; Saeed, M.; Xu, Z.; Zhong, F.; Song, R.; Huai, M.; Zheng, M.; Xie, C.; et al. Regulating glucose metabolism with prodrug nanoparticles for promoting photoimmunotherapy of pancreatic cancer. *Adv. Sci.* **2021**, *8* (4), 2002746.

(15) Yuan, Z. T.; Fan, G. H.; Wu, H. L.; Liu, C. L.; Zhan, Y. P.; Qiu, Y. Y.; Shou, C. T.; Gao, F.; Zhang, J.; Yin, P. H.; Xu, K. Photodynamic therapy synergizes with PD-L1 checkpoint blockade for immunotherapy of CRC by multifunctional nanoparticles. *Mol. Ther.* **2021**, *29*, 2931−2948.

(16) Wang, H.; He, Z.; Gao, Y.; Feng, D.; Wei, X.; Huang, Y.; Hou, J.; Li, S.; Zhang, W. Dual-pronged attack: pH-driven membrane-anchored NIR dual-type nano-photosensitizer excites immunogenic pyroptosis and sequesters immune checkpoint for enhanced prostate cancer photo-immunotherapy. *Adv. Sci.* **2023**, *10* (28), No. e2302422.

(17) Yang, W.; Liu, S.; Mao, M.; Gong, Y.; Li, X.; Lei, T.; Liu, C.; Wu, S.; Hu, Q. T-cell infiltration and its regulatory mechanisms in cancers: insights at single-cell resolution. *J. Exp. Clin. Cancer Res.* **2024**, *43* (1), 38.

(18) Anastas, J. N.; Moon, R. T. WNT signalling pathways as therapeutic targets in cancer. *Nat. Rev. Cancer* **2013**, *13*, 11−26.

(19) Luke, J. J.; Bao, R.; Sweis, R. F.; Spranger, S.; Gajewski, T. F. WNT/β-catenin pathway activation correlates with immune exclusion across human cancers. *Clin. Cancer Res.* **2019**, *25* (25), 3074−3083.

(20) Kimelman, D.; Xu, W. β-catenin destruction complex: insights and questions from a structural perspective. *Oncogene* **2006**, *25* (57), 7482−7491.

(21) Spranger, S.; Bao, R.; Gajewski, T. F. Melanoma-intrinsic β-catenin signalling prevents anti-tumour immunity. *Nature* **2015**, *523*, 231−235.

(22) Ganesh, S.; Shui, X.; Craig, K. P.; Park, J.; Wang, W.; Brown, B. D.; Abrams, M. T. RNAi-Mediated β-Catenin Inhibition Promotes T Cell Infiltration and Antitumor Activity in Combination with Immune Checkpoint Blockade. *Mol. Ther.* **2018**, *26*, 2567−2579.

(23) Huang, S. M. A.; Mishina, Y. M.; Liu, S.; Cheung, A.; Stegmeier, F.; Michaud, G. A.; Charlat, O.; Wiellette, E.; Zhang, Y.; Wiessner, S.; et al. Tankyrase inhibition stabilizes axin and antagonizes Wnt signalling. *Nature* **2009**, *461*, 614−620.

(24) Yamada, T.; Masuda, M. Emergence of TNIK inhibitors in cancer therapeutics. *Cancer Sci.* **2017**, *108*, 818−823.

(25) Zhan, L.; Zhang, J. H.; Zhu, S. D.; Liu, X. J.; Zhang, J.; Wang, W. Y.; Fan, Y. J.; Sun, S. Y.; Wei, B.; Cao, Y. X. N6-Methyladenosine RNA Modification: An Emerging Immunotherapeutic Approach to Turning Up Cold Tumors. *Front. Cell Dev. Biol.* **2021**, *9*, 736298.

(26) Kalinova, R.; Dimitrov, I. Functional Polyion Complex Micelles for Potential Targeted Hydrophobic Drug Delivery. *Molecules* **2022**, *27* (7), 2178.

(27) Oda, C. M. R.; Malfatti-Gasperini, A. A.; Malachias, A.; Pound-Lana, G.; Mosqueira, V. C. F.; Fernandes, R. S.; de Oliveira, M. C.; de Barros, A. L. B.; Leite, E. A. Physical and biological effects of paclitaxel encapsulation on distearoylphosphatidylethanolamine-polyethyleneglycol polymeric micelles. *Colloids Surf., B* **2020**, *188*, 110760.

(28) Zeng, L. J.; Hu, X. M.; Liu, Z. H.; Zheng, C. Q.; Miao, C. F.; Yao, L. Y.; Zhou, X. Preparation of a photodynamic supramolecular nanodrug targeting Wnt/β-catenin pathway. *Chin. J. Hosp. Pharm.* **2023**, *43*, 2763−2769.

(29) Guo, R.; Wang, S.; Zhao, L.; Zong, Q.; Li, T.; Ling, G.; Zhang, P. Engineered nanomaterials for synergistic photo-immunotherapy. *Biomaterials* **2022**, *282*, 121425.

(30) Garofalo, M.; Bertinato, L.; Staniszewska, M.; Wieczorek, M.; Salmaso, S.; Schrom, S.; Rinner, B.; Pancer, K. W.; Kuryk, L. Combination Therapy of Novel Oncolytic Adenovirus with Anti-PD1 Resulted in Enhanced Anti-Cancer Effect in Syngeneic Immunocompetent Melanoma Mouse Model. *Pharmaceutics* **2021**, *13*, 547.

(31) Wang, Z. C.; Sun, C.; Wu, H. J.; Xie, J. Z.; Zhang, T.; Li, Y. M.; Xu, X. L.; Wang, P. L.; Wang, C. Cascade targeting codelivery of ingenol-3-angelate and doxorubicin for enhancing cancer chemo-immunotherapy through synergistic effects in prostate cancer. *Mater. Today Bio* **2022**, *13*, 100189.

(32) Wu, S.; Zhu, C.; Tang, D.; Dou, Q. P.; Shen, J.; Chen, X. The role of ferroptosis in lung cancer. *Biomark. Res.* **2021**, *9* (1), 82.

(33) Liu, J.; Zhang, X. M.; Cheng, Y. J.; Cao, X. T. Dendritic cell migration in inflammation and immunity. *Cell. Mol. Immunol.* **2021**, *18*, 2461−2471.

(34) Notarbartolo, S.; Abrignani, S. Human T lymphocytes at tumor sites. *Semin. Immunopathol.* **2022**, *44*, 883−901.

(35) Abdeladhim, M.; Karnell, J. L.; Rieder, S. A. In or out of control: Modulating regulatory T cell homeostasis and function with immune checkpoint pathways. *Front. Immunol.* **2022**, *13*, 1033705.

(36) Mielcarska, S.; Kula, A.; Dawidowicz, M.; Kiczmer, P.; Chrabanska, M.; Rynkiewicz, M.; Wziatek-Kuczmik, D.; Swietochowska, E.; Waniczek, D. Assessment of the RANTES Level Correlation and Selected Inflammatory and Pro-Angiogenic Molecules Evaluation of Their Influence on CRC Clinical Features: A Preliminary Observational Study. *Medicina* **2022**, *58*, 203.

https://doi.org/10.1021/acsami.5c04799
ACS Appl. Mater. Interfaces XXXX, XXX, XXX−XXX